Apparent temperatures of neutron-poor and neutron-rich compound nuclei

A. B. McIntosh [1,*] K. Hagel,[1] L. A. McIntosh,[1] R. Wada [1] J. Gauthier,[1] P. J. Cammarata,[1,2] A. Keeler [1,2]
A. Abbott [1,2] A. Hannaman,[1,2] B. Harvey [1,2] A. Jedele,[1,2] Y. W. Lui,[1] L. W. May [1,3]
M. Sorensen [1,2] M. Youngs,[1,3] A. Zarrella,[1,2] and S. J. Yennello[1,2]

[1]*Cyclotron Institute, Texas A&M University, College Station, Texas, 77843, USA*
[2]*Chemistry Department, Texas A&M University, College Station, Texas, 77843, USA*
[3]*Physics Department, Texas A&M University, College Station, Texas, 77843, USA*

The possibility of the dependence of the nuclear caloric curve on neutron excess sets a limit on the accuracy of our knowledge of the nuclear equation of state, and thus impacts predictive capabilities of nuclear reaction and nuclear astrophysics models. To date, theoretical models have not reached consensus on the magnitude or sign on the asymmetry dependence. To provide constraints, we have measured evaporated particles and heavy residues for complete and incomplete fusion-evaporation reactions in inverse kinematics. The temperatures extracted from the observed light charged particles tend to favor higher temperatures for the neutron-rich fused systems, though they are near the limits of the systematic uncertainty. The present measurement may be used as an upper limit to constrain the asymmetry dependence of the nuclear caloric curve.

I. INTRODUCTION

The microscopic interaction between fundamental particles over the previous 13.8 billion years has shaped the universe, and our small world within it, into the form we observe it today. In most cases, explaining the properties of the universe, or various parts of it, need not start at the level of the quantum field theory; a level of approximation and abstraction appropriate to the system being studied should be employed. Excitations of quantum fields are dubbed fundamental particles. Certain fundamental particles can and must interact to form hadrons. Those sufficiently stable hadrons we call protons and neutrons combine as units to build atomic nuclei. Nuclei, along with electrons, can form atoms and molecules, and the underlying quantum fields of the strong and weak interactions can be reasonably ignored by researchers at this level of resolution. There is little need to use quantum mechanics in describing the functioning of a human circulatory system. However, to explain, mechanistically, *how* societies, creatures, living cells, or habitable planets came to be, the whole history of the universe is relevant, and the history of the universe explores every scale.

The current abundances of the chemical elements, the matter we observe most readily, is a result of nuclear fusion in stars as well as the process of nuclei successively capturing multiple nucleons in explosive or otherwise exotic environments. In these processes, the interaction of nucleons is an appropriate level of resolution, and from the "fundamental" interactions between nucleons, a number of collective properties emerge. One is the asymmetry energy, which describes the energy penalty for having an imbalance of neutrons and protons bound together; how this energy penalty depends on the local density impacts many astrophysical phenomena, and thus impacts the current chemical abundances. Nuclear temperature and nuclear pressure also emerge from the fundamental interaction of nucleons. Together, the relationship between the pressure, density, chemical potential, internal energy, and temperature constitute the nuclear equation of state (EoS) [1–4]. As the largest uncertainty at present in the EoS is the asymmetry energy, we explore the impact of neutron excess on correlations of thermodynamic quantities in order to better characterize the nuclear EoS. It is in this context that we here relate our most recent extraction of apparent nuclear temperatures as a function of excitation energy for systems with significantly different neutron excess.

II. BACKGROUND

The nuclear caloric curve describes the relationship between the temperature and excitation energy of atomic nuclei. Borderie and Frankland have recently published an insightful review [5]. The concept of temperature was first applied to atomic nuclei in 1937 by Bethe [6] and Weisskopf [7]. In 1987 Fabris *et al.* observed a plateau in the temperature as a function of excitation energy [8], suggestive of a transition. Over the subsequent years, nuclear temperatures were extracted for a range of nuclear collisions varying greatly in size; significant differences were observed between the measurements. In 2002, Natowitz *et al.* [9] compiled a broad array of caloric curve data and sorted it by mass. Viewed in this way, the data demonstrate that the temperature on the plateau of the caloric curve, and the excitation energy at which the caloric curve plateaus depends on the mass. The dependence of the plateau

on the mass is significant: Nearly 50% in temperature, and greater than a factor of 2 in E^*/A when comparing nuclei in the mass 30–60 region to those in the 180–240 region. The dependence was attributed to the role of Coulomb forces [9].

Having observed a mass (or charge) dependence, it was natural to investigate how the nuclear caloric curve might depend on neutron excess. Investigations were made at relativistic energies at GSI by Sfienti *et al.* [10] and at intermediate energy at TAMU by Wuenschel *et al.* [11]. A slight dependence of the temperatures on the neutron excess can seen in both experimental analyses, but the authors did not claim a dependence of the caloric curve beyond statistical and systematic uncertainty.

Meanwhile, theoretical models were employed to investigate how the caloric curve might depend on neutron excess. Besprosvany and Levit employed a hot liquid drop model to predict higher limiting temperatures for more neutron-rich nuclei [12]. Ogul and Botvina employed the statistical multifragmentation model to predict decreased critical temperatures for more neutron-rich nuclei [13]. Kolomietz *et al.* employed a thermal Thomas-Fermi model to predict a depressed and rounded approach to the plateau temperature from low excitation for more neutron-rich nuclei [14]. Hoel, Sobotka, and Charity predicted, with the mononuclear model, a slight decrease in the plateau temperature, but only for extremely neutron-rich nuclei [15]. Su and Zhang used an isospin-dependent variant of a quantum molecular dynamics model and found slightly higher temperatures for neutron-rich nuclei [16]. From a theoretical standpoint, some models indicate that an asymmetry dependence of the nuclear caloric curve is an important aspect of the EoS, but which ingredients in theoretical models are relevant to describing the asymmetry dependence correctly remains an open question.

To constrain this, we investigated nuclear temperatures in multifragmentation reactions at intermediate energies. In contrast to previous work, we reconstructed the hot quasiprojectile source using charged particles and free neutrons; this was possible with the 4π NIMROD array [17]. Then by selecting the neutron excess of the reconstructed source within a narrow range of mass, and plotting temperatures as a function of the excitation energy of the reconstructed source, we observed systematically higher temperatures for the less neutron-rich quasiprojectiles [18–20]. This dependence of the nuclear caloric curve was statistically significant. The dependence was also determined to be significant relative to any systematic uncertainty arising from the free neutrons [21] used in the source reconstruction (the dominant uncertainty).

Motivated by our result, Souza and Donangelo found the statistical multifragmentation model predicts higher temperatures for neutron-poor primary fragments [22], in agreement with our previous result. Additionally, Zhang *et al.* investigated photon production with a variant of quantum molecular dynamics and noted that hard photons produced after the initial stage of the reaction displayed slightly higher temperatures for neutron-rich systems [23].

Also motivated by our results, Huang *et al.* investigated multifragmentation reactions at intermediate energy with a series of beams and targets to look again for a dependence of temperatures on system asymmetry using a chemical probe

(Albergo ratio), and found no dependence [24]. Huang *et al.* also used the statistical multifragmentation model to calculate apparent temperatures with and without Coulomb forces. As a function of asymmetry with a constant charge selection no asymmetry dependence is observed (independent of Coulomb); as a function of asymmetry with a constant mass selection an asymmetry dependence is observed (but only if Coulomb forces are included); the magnitude of the dependence is similar to our previous result. Huang *et al.* conclude the Coulomb contribution dominates our previous result.

Among those who seek to constrain the EoS of nuclear matter, there is a clear and continuing interest in whether or not there is an asymmetry dependence to the nuclear caloric curve, and, if observable, how strong it is, and if too small to discern, how weak it must be.

We have set out to measure nuclear temperatures for systems of hot nuclei with varying neutron excess using a reaction mechanism and measurement device different from our previous study.

III. EXPERIMENT

A. Design

The present experiment is designed to focus on fusion-evaporation in inverse kinematics. In such a mechanism, the excitation energy of the compound nuclei may be calculated from kinematics and knowledge of the fraction of the target that fused with the projectile; the neutron excess of the compound nuclei is controlled by the neutron excess of the projectile, though with fluctuations depending on which target nucleons fuse to the projectile.

The projectiles were chosen to be ^{78}Kr and ^{86}Kr at energies of 15, 25, and 35 MeV/u to obtain heavy compound nuclei with significant difference in neutron excess and various excitation energies; we vary the system neutron excess without varying the charge. While a heavier projectile would have been also interesting, the highest beam energy would not have been possible. The target was chosen to be ^{12}C to have high probability of complete fusion, or high fraction of the target fused in incomplete fusion.

To determine the temperature, the light charged particles produced in the fusion evaporation reactions should be measured over a broad angular range. We use the forward array using silicon technology (FAUST) which provides coverage from $1.6°$ to $45.5°$, good energy resolution, and good position resolution. To determine the excitation energy, the velocity of very forward-focused fusion residues should be measured. We use the quadrupole triplet spectrometer (QTS), which uses fast timing detectors over a long flight path. To illustrate the appropriate coverage of FAUST+QTS for these reaction products, we used the heavy-ion phase-space exploration (HIPSE) event generator [25]. Figure 1 shows the velocity distribution ($v_\perp$ vs $v_\parallel$) for α particles produced in reactions of ^{86}Kr + ^{12}C at 15 MeV/u (top panel), at 25 MeV/u (middle panel), and at 35 MeV/u (bottom panel). The events are filtered for the acceptance (geometrical and kinetic) of the FAUST array and filtered for acceptance (geometrical and rigidity) of a residue in the QTS. The velocity of α particles is shown
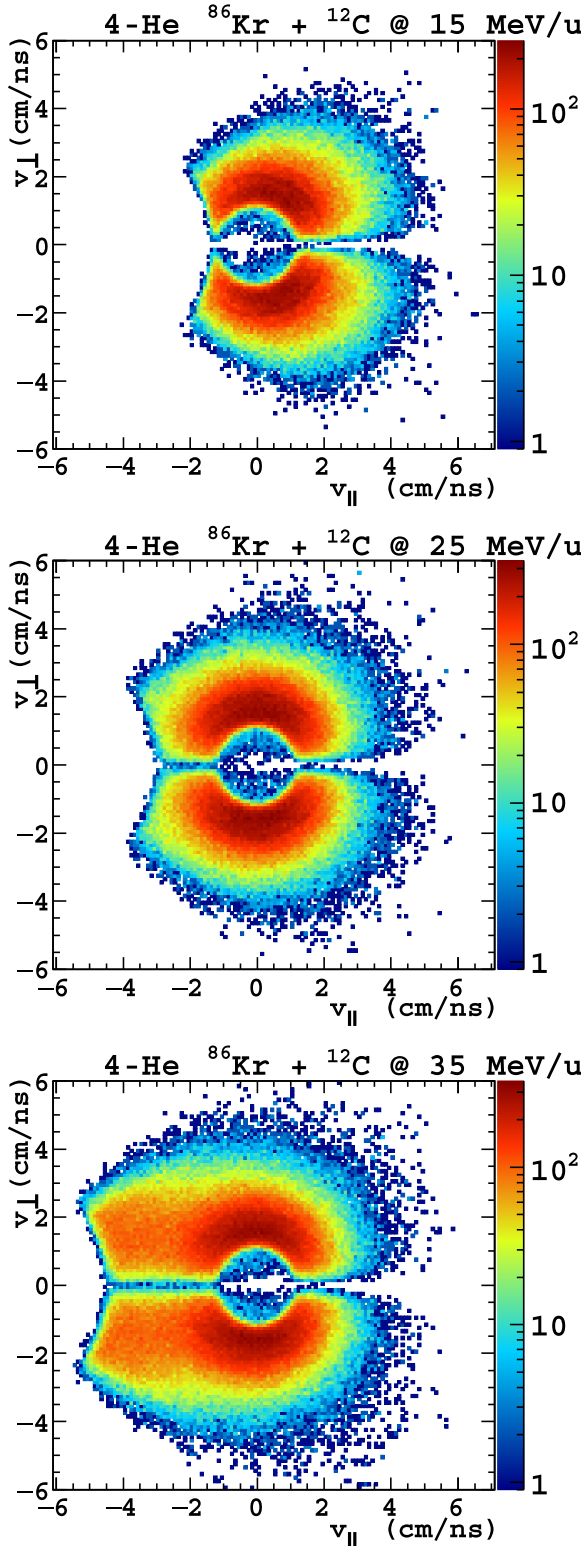
FIG. 1. Velocity distributions of α particles predicted by HIPSE for ^{86}Kr + ^{12}C at 15 MeV/u (top), at 25 MeV/u (middle), at 35 MeV/u (bottom).

in the frame of the coincident residue. The distributions are clearly centered at rest in the frame of the residue, and show a characteristic Coulomb hole and Coulomb ridge consistent

with evaporative emission from an excited highly charged source. At low $v_\parallel$, the distributions are abruptly truncated due to the threshold requirement that the evaporated α particle punch through the first layer (300 μm silicon) of the FAUST telescope. At large and at very small $v_\perp$, the distributions are truncated by the finite angular coverage of FAUST. That a large portion of the Coulomb ring is observed here in coincidence with a heavy residue shows that FAUST+QTS is suited to the task.

B. Execution

At the Texas A&M University Cyclotron Institute, beams of ^{78}Kr and ^{86}Kr were accelerated to 15, 25, and 35 MeV/u and impinged on 1 mg/cm^2 thick natural carbon targets. Complete fusion was expected to dominate the reaction cross section at 15 MeV/u, and incomplete fusion to dominate at 25 and 35 MeV/u. Neutron-rich compound nuclei are thus produced with the ^{86}Kr beam, and neutron-poor compound nuclei with the ^{78}Kr beam. The excitation energy depends on the fraction of the target that fuses with the Kr.

In order to verify the reaction mechanism and determine the excitation energy, the fusion-evaporation residues were measured by time of flight in the QTS [26]. Direct and elastically scattered beam was blocked out to 0.9°; reaction products outside this range and inside 2.3° are measured by time of flight between fast timing detectors separated by approximately 5.5 m. A parallel plate avalanche counter and a thin plastic scintillator were used at each end of the flight path, and data from the highest performing pair were used to calculate the time of flight. A quadrupole triplet is used to minimize loss along the flight path. For each of the six beams, the central rigidity of the QTS was adjusted to explore the distribution of residues, and data was obtained at multiple settings. For the majority of data collection, the QTS was tuned to the setting with the maximum yield. This corresponded to central magnetic rigidities of 1.10, 1.40, 1.66 Tm for the 15, 25, and 35 MeV/u ^{78}Kr beams, and 1.14, 1.48, and 1.78 Tm for the 15, 25, and 35 MeV/u ^{86}Kr beams.

The charged particles evaporated from the compound nuclei were measured in the FAUST array [27]. FAUST is comprised of 68 Si-CsI(Tl)/PD telescopes covering completely the angular range 2.3° to 34.5°, with partial coverage down to 1.6° and up to 45.5°. The silicon detectors of FAUST are dual axis duolateral (DADL) to achieve excellent position sensitivity. The signals of FAUST [28] were amplified with RisCorp (silicon) [29] or ZeptoSystems (CsI(Tl)+PD) [30] charge sensitive amplifiers, and shaped and digitized with the HINP3 ASIC [31] and the J-TEC model XLM-XXV universal logic module, respectively. The gain of the preamplifiers (110 mV/MeV for silicon, and 45 mV/MeV silicon-equivalent for CsI(Tl) + PD) was chosen to focus on light charged particles ($Z = 1, 2$) and lithium isotopes. The calibration of FAUST follows the procedure described previously [28,32]. The position of particles on the face of a DADL silicon detector is determined from the resistive charge splitting using the relative difference of the signal amplitudes from two contacts on a common face of the DADL. The position within a detector is known to better than 200 μm [33], and the relative
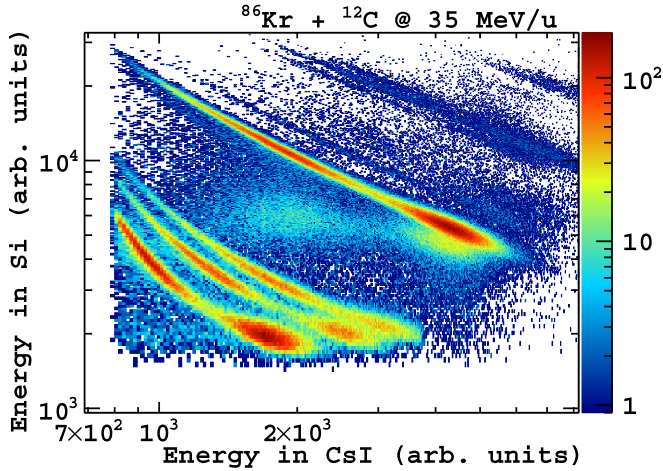
FIG. 2. Particle identification by ΔE-E in a representative detector (21) of FAUST.

FIG. 4. Velocity distributions of fusion-evaporation residues measured in the QTS in coincidence with a charged particle in FAUST. Top, from left to right: ^{78}Kr +C at 15, 25, 35 MeV/u; bottom, from left to right: ^{86}Kr +C at 15, 25, 35 MeV/u. The dotted and dashed lines matched to the height of the nearest distribution indicate the velocity of the beam and the velocity corresponding to complete fusion, respectively.

position of the detectors is determined from design specifications and verified with a precision slotted mask [28]. The energy deposited by charged particles in the silicon detector is calibrated relative to a ^{228}Th α source; an empirical correction is made [28] to the energy calibration as a function of position to correct for the pulse-shape distortion arising from the capacitive coupling of the uniformly resistive detector faces. An alternate and more sophisticated treatment using different electronics to compensate for this distortion is described by Aslin, Hannaman *et al.* [34,35]. A signal from any CsI detector of FAUST was used to trigger the data acquisition. Particle identification is achieved using the ΔE-E technique. Figure 2 shows, in log-log space, the energy lost in the silicon detector vs the remaining energy deposited in the CsI crystal. Each band corresponds to a different particle type. Starting from the bottom, protons, deuterons, tritons, and α particles show significant yield. A small but no less important yield of ^{3}He and ^{6}He can each be seen on either side of the alpha particles. Much of the distribution of the lithium isotopes can be seen higher up and to the right.

IV. ANALYSIS

A. Excitation energy

From FAUST alone, which triggered the data acquisition, we examine in the left panel of Fig. 3 the measured charged
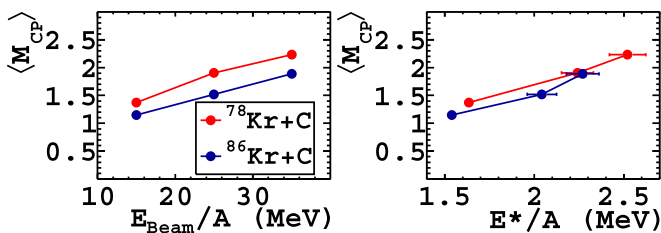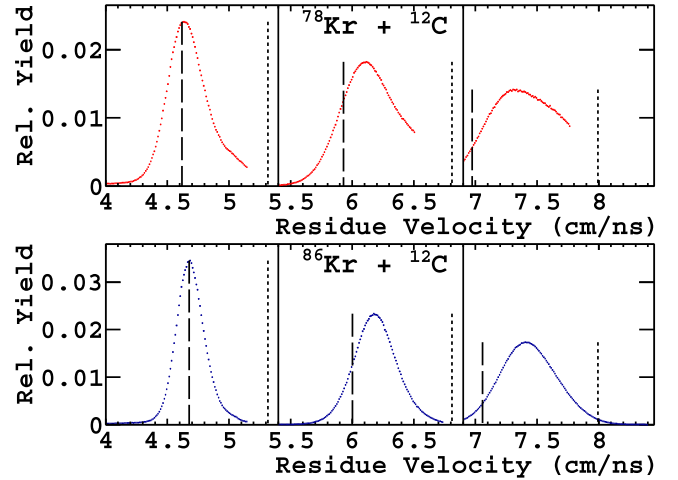

FIG. 3. Measured charged particle multiplicity in FAUST as a function of beam energy per nucleon (left) and excitation energy per nucleon (right) for ^{78}Kr +C (red) and ^{86}Kr +C (blue).

particle multiplicity as a function of the beam energy for the neutron-poor systems (^{78}Kr, red) and the neutron-rich systems (^{86}Kr, blue). As the beam energy increases, the excitation energy of the compound nucleus is expected to increase, and therefore the charged particle multiplicity is also expected to increase; this is borne out in the data. The neutron-poor systems show larger charged particle multiplicities than the neutron-rich systems. This is expected since the neutron-rich system is more likely to shed a larger fraction of its excitation energy in the form of free neutrons, consistent with predictions of the GEMINI++ model [36,37].

The average excitation energy is calculated from the velocity distribution of the heavy fusion-evaporation residue. Figure 4 shows the velocity distribution of residues measured in the QTS for the neutron-poor systems (top panel) and neutron-rich systems (bottom panel). Each distribution is accompanied by vertical dotted line and a vertical dashed line matched to the height of the peak. These two lines indicate the beam velocity and the velocity corresponding to complete fusion, respectively. All six distributions are peaked well away from the beam velocity and much closer to the fusion velocity. In the case of the 15 MeV/u systems, the peak is essentially at the fusion velocity, indicating that complete fusion dominates the cross section; the width of the peak reflects the kinematic recoil from evaporative emission. The QTS was tuned to maximize the yield for each system; the peaks of the velocity distributions reflect the most probable excitation energy. The velocity distributions for the higher energy systems indicate predominantly incomplete fusion; since the distributions are closer to fusion than beam velocity, more than half of the target fused with the projectile. The distributions, where evidently truncated, have indeed been gated to exclude events corresponding to elastically scattered beam. The widths of the distributions for the 25 and 35 MeV/u systems are

TABLE I. Excitation energies for the six systems studied.

Beam energy	Excitation energy	
	^{78}Kr	^{86}Kr
(MeV/u)	(MeV/u)	(MeV/u)
15	1.63	1.54
25	2.24	2.04
35	2.52	2.27

notably larger than for the 15 MeV/u systems; in addition to broadening due to kinematic recoil, the reaction mechanism includes fusion with various number of target nucleons. The most probable velocity thus reflects the weighted average.

From the peak velocity, we calculate the excitation energy for each system. This is done according to the formula presented by Bohne [38]:

$$\frac{E*}{m_R} = \frac{1}{2}(v_P - v_R)v_R + \frac{Q}{m_R}$$
$$+ \frac{1}{2}\frac{\Delta m_T}{m_R}(\cos(\theta_T)v_P - v'_T)v'_T, \quad (1)$$

where $E*$ is the excitation energy of the compound nucleus, m_R is the mass of the recoil (i.e., the compound nucleus), v_P and v_R are the projectile and recoil velocities, respectively, Q is the mass-energy released in the reaction (Q value), Δm_T is the mass of the target remnant, θ_T indicates the angle of the target remnant relative to the beam axis, and v'_T the velocity of the target remnant. The first term reflects conservation of energy and momentum for a complete or incomplete fusion reaction. The second term incorporates the mass energy gained or released, and the third the correction for the energy carried by the unfused remnant of the target. We have dropped Bohne's term for the energy carried by the unfused remnant of the projectile, since for this mass asymmetry, the krypton does not shed mass; the mass transfer occurs from the carbon to the krypton. This formula agrees precisely with that of Hagel [39] and Fabris [8] if one assumes the sudden approximation, i.e., the remnant of the target remains at rest.

Since the velocity imparted to the target remnant is unmeasured, this constitutes an important uncertainty in the excitation energy. If the remnant of the target is varied from 0% to 10% of the velocity of the evaporation residue, the deviation of the excitation energy per nucleon of the compound nucleus varies by ±4%. We take this spread to be our systematic error in excitation energy. This uncertainty is the dominant uncertainty in the excitation energy for the 25 and 35 MeV/u systems. The 15 MeV/u systems, which demonstrate complete fusion, naturally do not suffer this uncertainty. The excitation energies are reported in Table I.

The charged particle multiplicity is shown as a function of the excitation energy per nucleon in the right panel of Fig. 3. Naturally, the multiplicity rises with increasing excitation. The neutron-rich system displays lower charged particle multiplicity than the neutron-poor system; the explanation is the same as for the left panel: The neutron-rich system is more likely to shed a larger fraction of its excitation energy in the
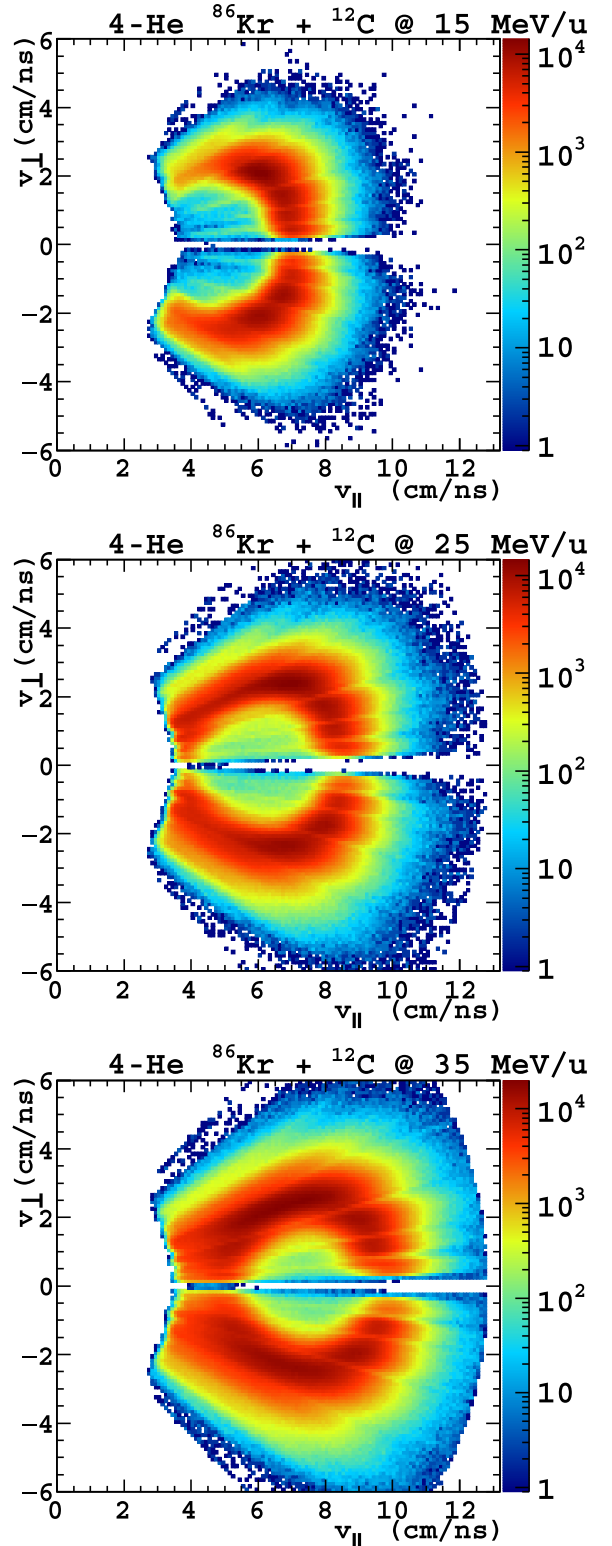

FIG. 5. Velocity spectra for α particles measured in FAUST for ^{86}Kr +C at 15 MeV/u (top), ^{86}Kr +C at 25 MeV/u (middle), and ^{86}Kr +C at 35 MeV/u (bottom).

form of free neutrons. The error bars in the excitation energy per nucleon reflect the systematic uncertainty arising from the uncertainty in the velocity of the target remnant.

B. Particle spectra

We now turn to the spectra of particles measured in FAUST. Figure 5 shows the yield vs $v_\perp$ vs $v_\parallel$ for all measured α particles for the ^{86}Kr systems at 15 MeV/u (top panel), at 25 MeV/u (middle panel), and at 35 MeV/u (bottom panel). Clearly visible in each is a significant portion of a Coulomb ring. Each ring is centered on a velocity clearly below the beam velocity and consistent with the peak velocity displayed in Fig. 4. This agreement of the two distributions, while triggering only on FAUST, supports the determination of the excitation energy. The velocity distributions in Fig. 5 are impacted at low $v_\parallel$ by the requirement that particles punch through the FAUST silicon into the CsI crystal, at high $v_\parallel$ by the requirement that particles not punch completely through the CsI crystal, and at low and high $v_\perp$ by the finite angular acceptance of FAUST.

A subset of the data shown in Fig. 5 are shown in Fig. 6, with the requirement that each α particle have a residue measured in coincidence in the QTS. In that case, the measured velocity of the residue is used as an approximation of the velocity of the compound nucleus, and the α particle velocity distributions are transformed into this frame. The distributions are quite similar. The yield is reduced by less than an order of magnitude, reflective of the combined probability of passing within the angular and rigidity acceptance of the QTS. The inner edge of the Coulomb hole is somewhat more pronounced in this frame, and the distributions are well centered on (0,0), both of which indicate that this frame is a good approximation of the true source frame. Superimposed on the data are black lines and arcs; within the region enclosed by two arcs and two lines on each plot, we have full kinematic coverage. This full energy distribution in this region can be used to calculate slope temperature. The clean shape of these distributions as a single-source Coulomb ring centered at velocities just below beam velocity and close to or at complete fusion velocity, and with a coincident residue near zero degrees with a velocity matching the Coulomb ring supports the picture of the reaction mechanism as either complete fusion followed by evaporation (15 MeV/u) or incomplete fusion followed by evaporation (25 and 35 MeV/u), as well as supporting the deduced excitation energy.

C. Calculation of temperatures

Temperatures are calculated according to three prescriptions. Two of them, slope temperatures and fluctuation temperatures, are kinetic methods; in principle, these are two ways of extracting the same information. The third is the Albergo temperature, a chemical method.

1. Slope temperature

To calculate the slope temperature, the kinetic energy distributions of particles in the frame of the source are used. Figure 7 shows the energy distribution of α particles for the neutron-rich system at 35 MeV/u in the frame of the measured residue. The uppermost distribution is integrated from 10° to 70° as indicated by the black lines in Fig. 6. The distribu-
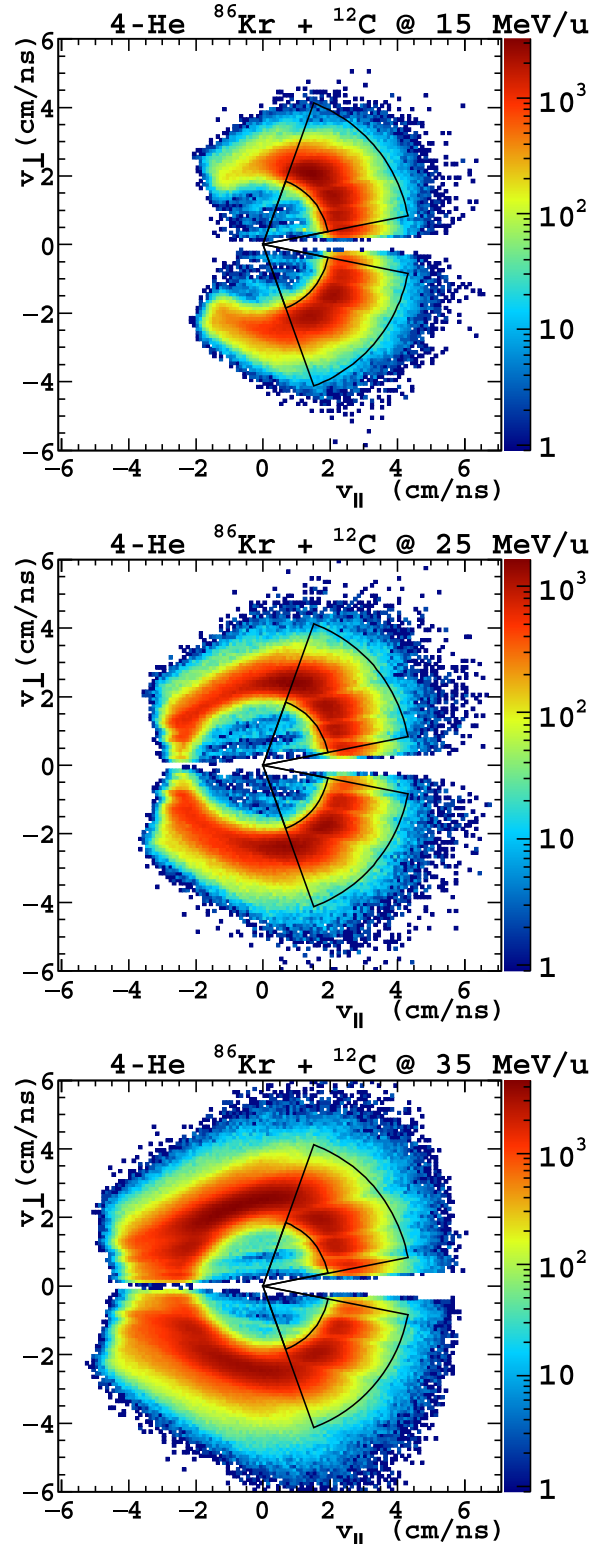

FIG. 6. Same as Fig. 5, with the requirement that a heavy residue be measured in coincidence in the QTS, and transforming the α particle velocity to the frame of the residue. Lines and arcs indicate the region of complete kinematic coverage used for subsequent Maxwell-Boltzman fits.
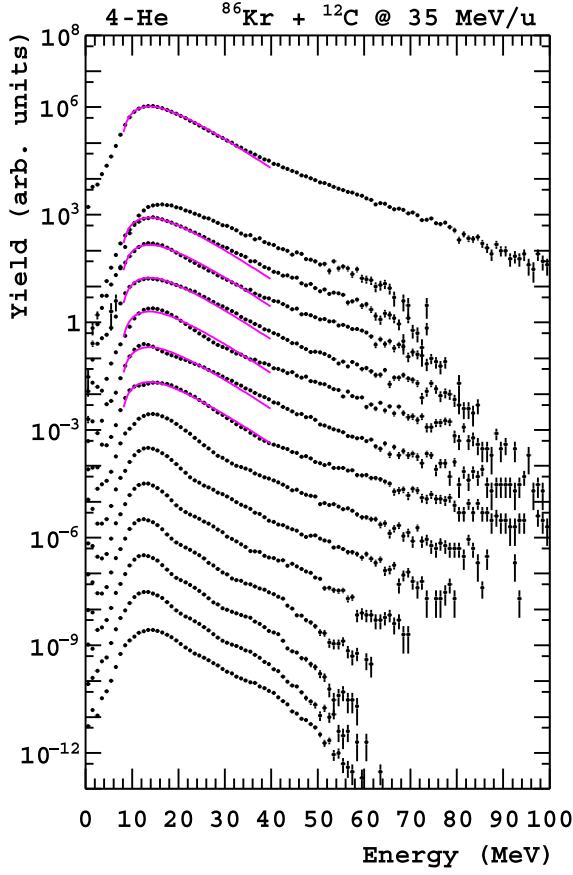
FIG. 7. Energy distributions of α particles in the frame of the co-incident evaporation residue for reactions of ^{86}Kr +C at 35 MeV/u. Uppermost distribution is summed from $10°$ to $70°$. Each distribution below this corresponds to an angular range $10°$ wide; from the top down: $0°$ to $10°$, $10°$ to $20°$, $20°$ to $30°$, etc. The magenta curve is a Maxwell-Boltzman with a diffuse barrier fit to the upper most data series, and scaled and superimposed on top of the distributions that comprise it.

tions below each correspond to a narrow $10°$-wide window of integration; from top to bottom: $0°$ to $10°$, $10°$ to $20°$, $20°$ to $30°$, $30°$ to $40°$, and so on. The distributions from $10°$ to $70°$ all have very similar shapes, and beyond this region, deviations appear due to the finite geometrical coverage. A Maxwell-Boltzmann fit with a diffuse barrier is applied to the integrated $10°$ to $70°$ distribution. The functional form [40] of the yield as a function of energy is

$$Y(E) = 0; E < B',$$

$$Y(E) \propto C'(E - B')^D \exp\left(\frac{-E}{T}\right); B' < E < B+T, \quad (2)$$

$$Y(E) \propto (E - B) \exp\left(\frac{-E}{T}\right); E \geqslant B+T,$$

where $C' = T/(DT)^D$ and $B' = (1 - D)T + B$. The measured yield $Y(E)$ is given as a function of kinetic energy E. The height of the barrier is described by B, while D represents the barrier diffuseness and penetrability. The temperature T
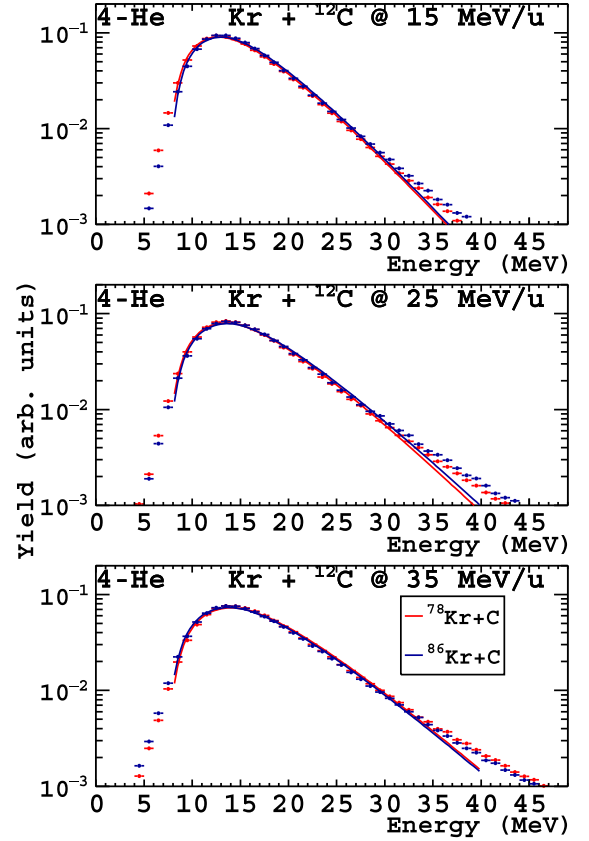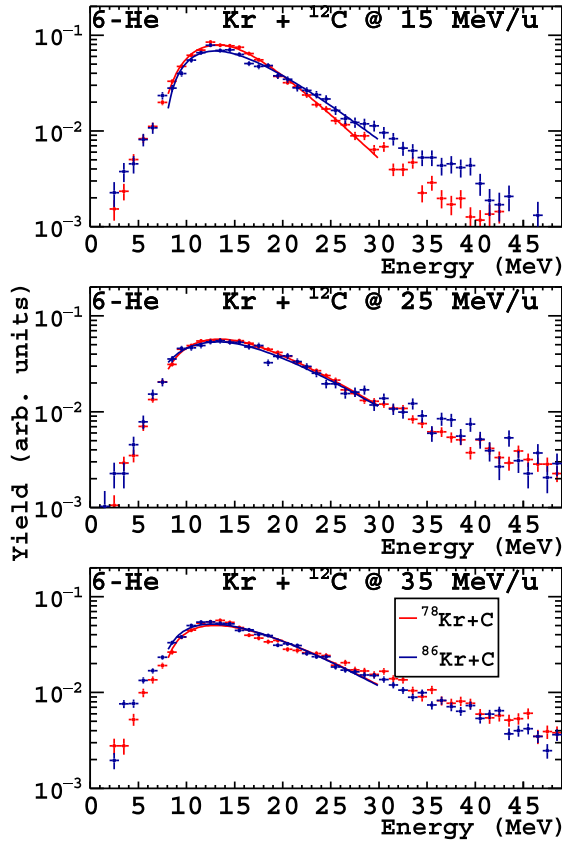

FIG. 8. α particle kinetic energy spectra in the frame of the evaporation residue for ^{78}Kr +C (red) and ^{86}Kr +C (blue) at 15 MeV/u (top), at 25 MeV/u (middle), at 35 MeV/u (bottom). Curves show Maxwell-Boltzmann fits with diffuse barriers.

characterizes the exponential slope of the kinetic energy distribution. The result of the fit is indicated by the magenta curve, and describes the peak and the exponential fall of the distribution for about one and a half decades. At high energy, the distribution is dominated by pre-equilibrium emission; as this portion does not reflect the thermal characteristics of the equilibrated system, we exclude it from the fit. The distribution is scaled and superimposed over the $10°$-wide distributions below that comprise it, to indicate the agreement of the shape.

Figure 8 shows the α particle energy distributions and their fits for all six systems; blue data and curves correspond to the neutron-rich system, and red to the neutron-poor. The upper panel shows the 15 MeV/u systems, the middle panel the 25 MeV/u systems, and the lower panel the 35 MeV/u systems. Each distribution is normalized to an area of 1. The distributions become harder (more energetic particles) with increasing beam energy. All are well described by the Maxwell-Boltzmann fit for at least one and a half decades of exponential fall. The spectra and their resulting fits, and temperatures are nearly identical for systems at the same beam energy.

Figure 9, similar to the previous figure, shows kinetic energy spectra for ^{6}He nuclei in the forward angular range in the frame of the measured residue. Again, the slopes become harder as beam energy increases. In this case, however, there is a slight dependence of the slope on the neutron-richness.
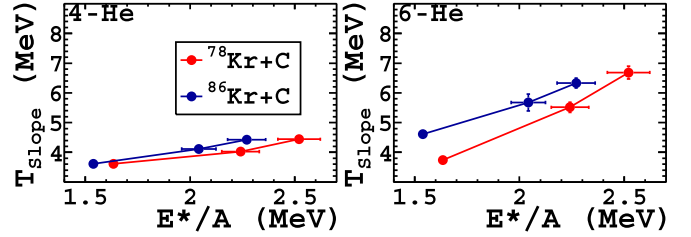
FIG. 9. Same as Fig. 8 but for ^{6}He nuclei.

FIG. 10. Slope temperatures for α particles (left) and ^{6}He nuclei (right) for ^{78}Kr +C (red) and ^{86}Kr +C (blue).

of $Q_{xy} = p_x^2 - p_y^2$ is calculated for each particle type for each system. The variance of the Q_{xy} distribution is related to the temperature by $\langle \sigma_{xy}^2 \rangle = 4m^2 T^2$.

3. Chemical temperature

Temperatures are also extracted from particle double yield ratios according to the method of Albergo *et al.* [42], which describes the yield of particular clusters of nucleons in equilibrium as arising from the ground state binding energies and spin degeneracies according to $T_{\text{raw}} = \frac{B}{\ln(aR)}$, where B is a double difference of binding energies, a is a double ratio of spin degeneracies, and R is a double isotopic yield ratio. We include a correction for secondary decay as described by Xi *et al.* [43] as $T = \frac{1}{\frac{1}{T_{\text{raw}}} - \frac{\ln(\kappa)}{B}}$. It is understood that certain kinetic thermometers may differ from chemical thermometers due to a variety of factors such as the Fermi motion of nucleons (see, e.g., Refs. [44,45]). We apply this prescription for completeness, though we are applying it at the limit of its applicability. The method assumes the clusters arise from a clustering of nucleons in an equilibrium process; in this fusion evaporation measurement, the clusters come off sequentially from a large source which is not necessarily far from saturation density.

D. Correlation of temperature with excitation

We now correlate the temperatures (extracted in the ways described in Sec. IV C) to the excitation energies (as calculated in Sec. IV A).

We begin with the slope temperatures. Figure 10 shows the slope temperatures for ^{4}He (left panel) and ^{6}He (right panel) as a function of excitation energy for the neutron-rich systems (blue) and the neutron-poor systems (red). The temperatures rise with increasing excitation. For the α particles, the neutron-rich systems display nearly identical temperatures to the neutron-poor. There is a systematic difference in the excitation energies between the rich and poor, with the neutron-rich at lower excitation. The magnitude of this shift is on the order of the systematic error on the excitation energy, which arises from the uncertainty in the velocity of the target remnant. The behavior of the target remnant may be similar for the neutron-rich and neutron-poor systems; that is, if the remnant is 5% of the velocity of the residue in one system, it should be 5% the velocity of the residue in the other system. This would lead us to conclude that the relative spacing in E^*/A between the two systems is considerably more accurate than the absolute E^*/A value of either. The spacing can be described as a difference in E^*/A of 0.2 MeV or less, or as a

At 15 MeV/u, the neutron-rich systems display a slightly harder slope, both in the measured distribution and the fit that describes the data.

We do not here fit the kinetic distributions of $Z = 1$ particles. While these particles do show Coulomb rings centered around the measured residues, there is a complication in fitting their spectra obtained in FAUST. Because the DADL detectors measure position and energy by resistively splitting charge, the hydrogen isotopes, which deposit little energy in the silicon, only cause a signal to pass threshold if the split charge is sufficiently large. A slow proton which deposits moderate energy can pass threshold anywhere, but a fast proton can only pass threshold if it hits near the center of the detector. In effect, the detector efficiency (or more accurately, the effective active area) is energy dependent for $Z = 1$. Some of this is recoverable, but for the purposes of a smooth energy distribution which reflects the temperature accurately, the recovery is not yet adequate. However, for the purposes of particle correlations, the measured $Z = 1$ particles are perfectly usable. For application with the fluctuation thermometer, the $Z = 1$ particles are also usable, since the reduced efficiency applies to all detectors and the detectors are arranged symmetrically about the beam axis.

2. Fluctuation temperature

We also calculate temperatures according to the momentum quadrupole fluctuation (MQF) method set out by Zheng and Bonasera [41]. The momentum quadrupole distribution

temperature difference of less than 0.5 MeV. For the ^{6}He, the temperatures are higher than for ^{4}He; the more exotic particle is emitted on average earlier in the cascade. For the ^{6}He, we see the higher temperatures of the neutron-rich system and the higher E^*/A of the neutron-poor system provide somewhat more spacing between the two curves than we saw for ^{4}He. The neutron-rich system may emit more readily neutron-rich species initially, and the relative spacing may reflect an emission-time ordering.

GEMINI++ calculations were performed for the compound nuclei produced in these fusion evaporation reactions, according to the measured mass transfer [37]. The spin of the compound nuclei was varied from $0\hbar$ to the critical angular momentum for fusion, $45\hbar$. Within GEMINI++, the temperature for any specific excitation energy is calculated as $T = \sqrt{E/a}$, where $a = A/k$ and k is a parameter independent of neutron excess; therefore, the GEMINI++ model does not predict temperatures to depend on neutron excess. To investigate the impact of emission order and Coulomb repulsion, temperatures were extracted in the same fashion as in the experimental data, i.e., using the emitted light charged particles. For some particle types (α particles, deuterons, protons), there is no discernible difference in the slope temperature for neutron-rich and neutron-poor systems. For other particle types the temperatures for the neutron-rich systems are higher by 0.2 MeV (neutrons) or 0.4 MeV (tritons and ^{6}He, but only at low spin). These spacings of the temperature are, therefore, generated by the slope thermometer method, but do not reflect the internal temperature. It appears that the emission ordering of the neutron-rich isotopes from the neutron-rich species displays higher temperatures in agreement with the experimental data in Fig. 10. The observed difference between the ^{6}He slope temperatures for the neutron-rich and neutron-poor systems is comparable to the predictions of GEMINI++, and therefore is consistent with emission time ordering. Since GEMINI predicts no difference in the T vs E^*/A correlation for α particles emitted from the neutron-poor and neutron-rich compound nuclei formed in these reactions, the modest difference in the experimental data therefore cannot be attributed to emission time ordering.

The temperatures shows in Fig. 10 include all particles that have been emitted from the compound nuclei at all stages of de-excitation, and so the temperature is an average over the de-excitation cascade. Hagel *et al.* [46] describe a simple method to extract the primary temperature using the cascade-averaged temperatures and multiplicity. Since the measured multiplicity includes particles from the entire cascade, the primary temperature T' at a given excitation energy E_2^*/A which is slightly higher than E_1^*/A is approximated by

$$\langle T' \rangle = \frac{\langle T_2 \rangle \langle M_2 \rangle - \langle T_1 \rangle \langle M_1 \rangle}{\langle M_2 \rangle - \langle M_1 \rangle}, \tag{3}$$

where M_2 and M_1 are the measured multiplicities and T_2 and T_1 are the cascade-averaged temperatures at those excitation energies.

Figure 11 shows the primary slope temperatures extracted using Eq. (3). Naturally, the primary temperatures are higher than the average temperatures. For both ^{4}He and ^{6}He, the

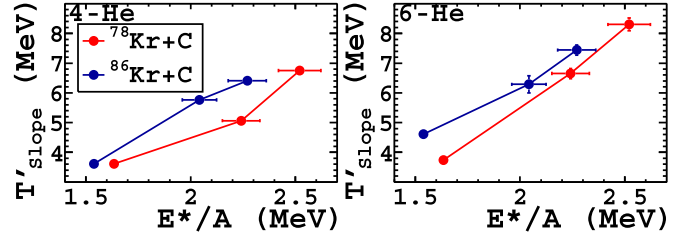FIG. 11. Primary slope temperatures for alpha particles (left) and ^{6}He nuclei (right) for ^{78}Kr +C (red) and ^{86}Kr +C (blue).

neutron-rich systems exhibit a systematic displacement toward lower E^*/A and higher primary temperature. For ^{4}He, the displacement between the systems is greater for the primary temperatures than for the average temperatures. For ^{6}He, the displacement between the systems is similar for the primary temperatures and the average temperatures. The cascade averaging is neither creating nor destroying the asymmetry dependence.

Figure 12 shows the correlation between the MQF temperature and the excitation energy for isotopes of hydrogen and helium. Again, neutron-rich systems are shown in blue, and neutron-poor systems in red. For some evaporated particles (^{2}H, ^{3}H, ^{6}He) there is no significant difference between the neutron-poor and neutron-rich systems. For ^{1}H, ^{3}He, and ^{4}He, the neutron-rich systems exhibit slightly higher temperatures. Again, the magnitude of the shift is close to the systematic uncertainty due to the target remnant. GEMINI++ calculations show slightly higher temperatures for the neutron-rich system for ^{3}He, and ^{4}He (though not ^{1}H), and the magnitude
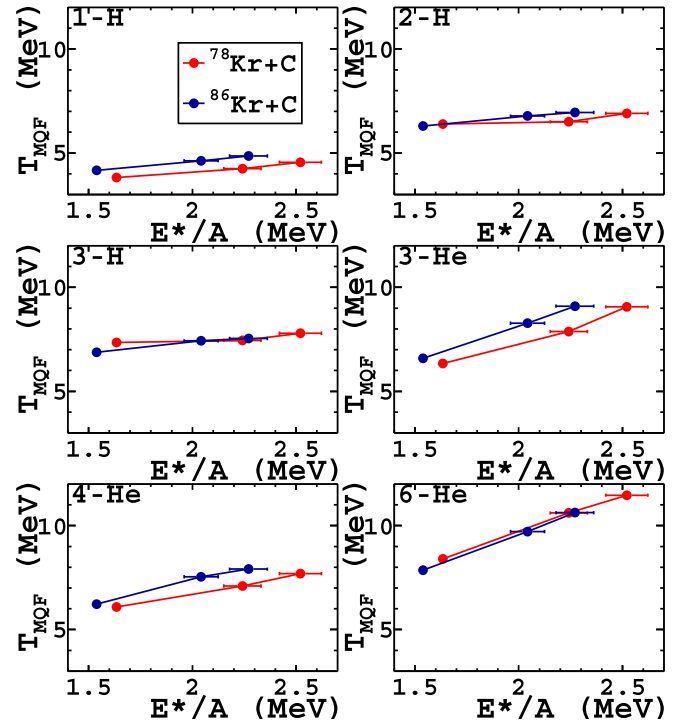

FIG. 12. In reading order of panels: MQF temperatures for protons, deuterons, tritons, helions, α particles, and ^{6}He nuclei for ^{78}Kr +C (red) and ^{86}Kr +C (blue).
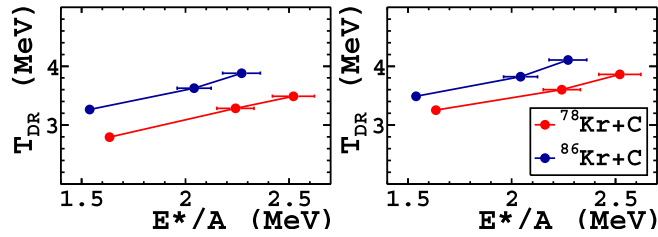
FIG. 13. Albergo temperatures for $\{p, d, h, a\}$ (left) and $\{d, t, h, a\}$ (right) for ^{78}Kr +C (red) and ^{86}Kr +C (blue).

is similar to that observed in the experiment. This indicates that the experimentally observed temperature spacing for ^{3}He, and ^{4}He (but not ^{1}H), originates from the MQF thermometer.

Figure 13 shows the Albergo temperatures as a function of excitation energy for $(p/d)/(h/a)$ in the left panel and $(d/t)/(h/a)$ in the right panel. Both show an increase in temperature as excitation increases. The apparent temperatures are higher for the neutron-rich systems in both cases. The Albergo temperatures were examined as a function of the polar angle in the frame of the residue, and found to be constant within the range 50° to 120°; the data in Fig. 13 therefore is integrated over this angular range. At smaller angles, the efficiency for measuring the hydrogen isotopes is reduced due to charge splitting on the DADL detector faces. At backward angles, the geometric coverage cuts the velocity distributions at the same cone in velocity space, but this corresponds to different surface velocities of the particles, which in this case introduces a systematic error beyond about 120°. Within this range of 50° to 120°, the behavior of the temperature with angle is constant, the behavior of the temperature with E^*/A is rising, and the neutron-rich systems show a systematically higher temperature. GEMINI calculations predict no dependence of the T vs E^*/A correlation on the neutron excess for these Albergo temperatures; the difference observed in the experimental data cannot be attributed to emission order or any other features of the GEMINI++ model.

It is worth mentioning that for all thermometers, the dependence of the extracted temperatures depend only weakly (for 25 and 35 MeV/u beams) or not at all (15 MeV/u beams) on the velocity of the residues measured event by event. This is consistent with recoil effects contributing to a significant part of the width of the residue velocity distribution. The variation of the temperatures with residue velocity within a system is small compared to the variation of temperatures with E^*/A between different systems. This again tells us that the most probable residue velocity well represents the ensemble, and thus is appropriate to use to calculate the excitation energy.

V. SUMMARY

We have measured fusion residues and evaporated light charged particles produced in reactions of ^{78,86}Kr +C at 15, 25, 35 MeV/u using FAUST and the QTS. We use the residues to calculate the excitation energy, and the light charged particles to calculate the temperature for each of the six reaction systems. The dominant uncertainty in the extracted T vs E^*/A correlations is the systematic uncertainty that arises from the unmeasured small remnant of the target.

For the ^{4}He slope temperature, an asymmetry dependence is seen in the experimental (both cascade-average and primary) temperatures, but is not seen in GEMINI++; this is consistent with a dependence of the caloric curve on neutron excess. For the ^{6}He slope temperature, an asymmetry dependence is seen in the experimental (both cascade-average and primary) temperatures, but is also seen in GEMINI++ to the same magnitude; thus the dependence observed in the experimental data may not reflect any dependence of the caloric curve on neutron excess.

For ^{2}H, ^{3}H, and ^{6}He MQF temperatures, no asymmetry dependence is seen in the measured data. For ^{3}He and ^{4}He, an asymmetry dependence is seen in the measured data, but is also observed in GEMINI++ to the same magnitude, and so the observed asymmetry dependence may not reflect any dependence of the caloric curve on neutron excess. For ^{1}H, an asymmetry dependence is seen in the measured data, but is not seen in GEMINI++; this is consistent with a dependence of the caloric curve on neutron excess.

For both Albergo thermometers, $(p/d)/(h/a)$ and $(d/t)/(h/a)$, an asymmetry dependence of the temperature is measured and no asymmetry dependence is seen in the GEMINI++ model; thus, the measured asymmetry dependence may reflect a true asymmetry dependence of the caloric curve.

Combined, this measurement contains some temperature probes which do not exhibit an asymmetry dependence, some temperature probes which do exhibit an asymmetry dependence which can be explained by the GEMINI++ model (either by emission order or differential Coulomb effects), and some temperature probes which exhibit an asymmetry dependence that is beyond what the GEMINI++ model can predict. This latter class suggests that there may be an asymmetry dependence of the caloric curve, though it is not seen in all probes. Since an asymmetry dependence is not seen for all probes, the observed dependence in this measurement can be characterized as an upper bound on the true asymmetry dependence of the caloric curve for $E^*/A < 3$ MeV.

The present work is consistent with previous measurements which show a very slight preference for higher temperatures for neutron rich systems but which are still consistent with no asymmetry dependence within uncertainties [10,11]. The present work is also consistent with measurements which exhibit, due to Coulomb effects, lower temperatures for neutron rich systems [18–20,24].

Some theoretical model calculations agree with the present observations. The SMM [13,22], QMD [16,23], and hot liquid drop models [12] predict, assuming no Coulomb differences, slightly higher temperatures for more neutron rich systems. Within the range of asymmetry probed, the mononuclear model [15] predicts no significant asymmetry dependence. Only the thermal Thomas-Fermi model [14] predicts a notably lower temperature for a neutron rich system, but this is only over a moderate range of excitation and even then depends on the pressure chosen for the calculation. With the level of sensitivity achieved, the present results are consistent with the magnitude and direction of the asymmetry dependence of the caloric curve predicted by SMM, QMD, hot LDM, and the mononuclear model.

ACKNOWLEDGMENTS

[1] H. T. Janka *et al.*, Phys. Rep. **442**, 38 (2007).

[2] P. Danielewicz, R. Lacey, and W. G. Lynch, Science **298**, 1592 (2002).

[3] B. A. Li, L. W. Chen, and C. M. Ko, Phys. Rep. **464**, 113 (2008).

[4] J. M. Lattimer and M. Prakash, Science **304**, 536 (2004).

[5] B. Borderie and J. Frankland, Prog. Part. Nucl. Phys. **105**, 82 (2019).

[6] H. A. Bethe, Rev. Mod. Phys. **9**, 69 (1937).

[7] V. Weisskopf, Phys. Rev. **52**, 295 (1937).

[8] D. Fabris *et al.*, Phys. Lett. B **196**, 429 (1987).

[9] J. B. Natowitz, R. Wada, K. Hagel, T. Keutgen, M. Murray, A. Makeev, L. Qin, P. Smith, and C. Hamilton, Phys. Rev. C **65**, 034618 (2002).

[10] C. Sfienti *et al.*, Phys. Rev. Lett. **102**, 152701 (2009).

[11] S. Wuenschel *et al.*, Nucl. Phys. A **843**, 1 (2010).

[12] J. Besprosvany and S. Levit, Phys. Lett. B **217**, 1 (1989).

[13] R. Ogul and A. S. Botvina, Phys. Rev. C **66**, 051601(R) (2002).

[14] V. M. Kolomietz, A. I. Sanzhur, S. Shlomo, and S. A. Firin, Phys. Rev. C **64**, 024315 (2001).

[15] C. Hoel, L. G. Sobotka, and R. J. Charity, Phys. Rev. C **75**, 017601 (2007).

[16] J. Su and F. S. Zhang, Phys. Rev. C **84**, 037601 (2011).

[17] S. Wuenschel *et al.*, Nucl. Instrum. Methods Phys. Res. A **604**, 578 (2009).

[18] A. B. McIntosh *et al.*, Phys. Lett. B **719**, 337 (2013).

[19] A. B. McIntosh *et al.*, Phys. Rev. C **87**, 034617 (2013).

[20] A. B. McIntosh *et al.*, Eur. Phys. J. A **50**, 35 (2014).

[21] P. Marini *et al.*, Nucl. Instrum. Methods Phys. Res. A **707**, 80 (2013).

[22] S. R. Souza and R. Donangelo, Phys. Rev. C **97**, 054619 (2018).

[23] F. Zhang *et al.*, Eur. Phys. J. A **54**, 180 (2018).

[24] Y. Huang *et al.*, Phys. Rev. C **101**, 064603 (2020).

[25] D. Lacroix, A. VanLauwe, and D. Durand, Phys. Rev. C **69**, 054604 (2004).

[26] P. Cammarata *et al.*, Nucl. Instrum. Methods Phys. Res. A **792**, 61 (2015).

[27] F. Gimeno-Nogues *et al.*, Nucl. Instrum. Methods Phys. Res. A **399**, 94 (1997).

[28] L. A. Heilborn, Ph.D. thesis, Texas A&M University, 2018.

[29] R. Todd, Ris-corp, 5905 Weisbrook Lane, Suite 102 Knoxville, TN 37909.

[30] R. de Souza, Zeptosystems, Bloomington, IN 47401.

[31] G. Engel *et al.*, Nucl. Instrum. Methods Phys. Res. A **573**, 418 (2007).

[32] L. A. McIntosh *et al.*, Nucl. Instrum. Methods Phys. Res. A **985**, 164642 (2021).

[33] S. N. Soisson *et al.*, Nucl. Instrum. Methods Phys. Res. A **613**, 240 (2010).

[34] M. W. Aslin *et al.*, Nucl. Instrum. Methods Phys. Res. A **985**, 164674 (2021).

[35] A. Hannaman *et al.* [Nucl. Inst. Meth. A (to be published)].

[36] R. J. Charity, GEMINI A code to simulate the decay of a compound nucleus by a series of binary decays (INDC(NDS)–0530), edited by G. Mank (International Atomic Energy Agency, Austria, 2008).

[37] R. J. Charity, Phys. Rev. C **82**, 014610 (2010).

[38] W. Bohne, H. Morgenstern, K. Grabisch, T. Nakagawa, and S. Proschitzki, Phys. Rev. C **41**, R5 (1990).

[39] J. C. Hagel, Ph.D. thesis, Texas A&M University, 1896.

[40] R. Yanez *et al.*, Phys. Rev. C **68**, 011602(R) (2003).

[41] H. Zheng and A. Bonasera, Phys. Lett. B **696**, 178 (2011).

[42] S. Albergo, S. Costa, E. Costanzo, and A. Rubbino, Il Nuovo Cimento **89**, 1 (1985).

[43] H. Xi, W. G. Lynch, M. B. Tsang, W. A. Friedman, and D. Durand, Phys. Rev. C **59**, 1567 (1999).

[44] W. Bauer, Phys. Rev. C **51**, 803 (1995).

[45] A. Kelic, J. B. Natowitz, and K. H. Schmidt, Eur. Phys. J. A **30**, 203 (2006).

[46] K. Hagel *et al.*, Nucl. Phys. A **486**, 429 (1988).